Analytic bond-order potential for bcc and fcc iron—comparison with established embedded-atom method potentials

Michael Müller, Paul Erhart and Karsten Albe

Institut für Materialwissenschaft, Technische Universität Darmstadt, D-64287 Darmstadt, Germany

E-mail: mueller@mm.tu-darmstadt.de

Abstract
A new analytic bond-order potential for iron is presented that has been fitted to experimental data and results from first-principles calculations. The angular-dependent functional form allows a proper description of a large variety of bulk, surface and defect properties, including the Bain path, phonon dispersions, defect diffusivities and defect formation energies. By calculating Gibbs free energies of body-centred cubic (bcc) and face-centred cubic (fcc) iron as a function of temperature, we show that this potential is able to reproduce the transitions from α-iron to γ-iron and δ-iron before the melting point. The results are compared to four widely used embedded-atom-method potentials for iron.

(Some figures in this article are in colour only in the electronic version)

1. Introduction

Atomic-scale simulations are nowadays a standard tool in condensed matter physics, chemistry and materials science. They enable a detailed investigation of material processes and phenomena with atomic resolution. The outcome of atomistic simulations is, however, largely dependent on a realistic description of the interatomic interactions. Quantum-mechanical codes based on first-principles methods, like density-functional theory (DFT), have become widely available over the last decade, but they are computationally demanding and therefore limited to small system sizes. Simulations of extended systems on long timescales are therefore only possible if interatomic potentials are used. These are computationally more efficient, because the electronic degrees of freedom are not explicitly treated and the energy of a system is solely described by the positions of the constituent atoms. In the hierarchy of modelling techniques, atomistic simulations with analytic interatomic potentials close the gap between

self-consistent quantum-mechanical calculations and coarse-grained methods based on quasi-particle or continuum models. In the realm of metallic materials the embedded-atom method (EAM) [1] and its variants [2, 3] have been successfully applied for describing materials properties of various d transition metals. Modelling of magnetic materials, including iron, has, however, remained a true challenge. Iron exhibits a phase transition between bcc α-iron and fcc γ-iron at $T_c^{\alpha\gamma} = 1184$ K, and a transition back to the bcc phase (δ-iron) at $T_c^{\gamma\delta} = 1665$ K before melting [4]. The origin of these phase transitions is well understood [5]: the contribution of ferromagnetic energy to the total energy of the bcc phase stabilizes α-iron over γ-iron at low temperatures. Also, the degrees of freedom of the magnetic spins represent the decisive contributions to the entropies of the bcc and fcc phases, leading to the α to γ transition at $T_c^{\alpha\gamma}$ and γ to δ transition at $T_c^{\gamma\delta}$, while the vibrational contributions to the entropy are only of secondary importance.

In molecular dynamics (MD) simulations, however, where the classical trajectories of atoms are calculated, the dynamics of the electronic subsystem is missing. Therefore it is conceptually challenging to model phase transitions, where spin contributions become decisive, by MD simulations.

In the past, a large variety of interatomic potentials for Fe and some of its alloys have been proposed [6–12], most of them relying on a central force description. Angular-dependent potentials were developed within the modified EAM [13], the embedded-defect method (EDM) [14] and the angular-dependent potential method (ADP) [15], which allow an improved description of a number of properties as compared to standard EAM potentials. Interestingly, to the best of our knowledge transitions between the α- and γ-phases have only been considered in pure iron in [9] and in the context of martensite–austenite transitions in Fe–Ni alloys [8]. Recently, Dudarev and Derlet [11] proposed a potential in which magnetic contributions are included via a Stoner model. They present two separate parameterizations of their potential for magnetic and non-magnetic iron phases, but do not address the problem of how to switch from one to the other with increasing temperature.

In this paper, we introduce a new angular-dependent analytic bond-order potential (ABOP) for iron, which reproduces the α–γ–δ–liquid phase sequence. The functional form of this potential has been successfully applied for modelling other transition metals, including platinum [16] and bcc tungsten, as well as tungsten carbide [17] and various other compounds, before (see e.g. [18]).

In case of iron, the Gibbs free energy difference between the bcc phase and the fcc phase is dominated by energy and entropy contributions of the spin system. The key idea of our approach is to mimic this difference by lattice energy and phonon contributions, only. This is done by adjusting the lattice energy difference of the bcc and fcc phases in a way that the calculated Gibbs free energies cross at the desired temperatures. The potential thus obtained is then applicable for problems in which the bcc–fcc transition is of importance. This interatomic potential, in a sense, counterbalances the fact that electronic degrees of freedom are missing in classical molecular dynamics simulations.

In addition, we provide a thorough comparison of the ABOP with four established iron potentials, including the EAM potential by Simonelli *et al* (potential 'A' in [6]), the Fe part of the Fe–Cu potential by Ackland *et al* [7], the Mendelev *et al* potential (parameterization II) [10] and the 'magnetic' potential of case study II of Dudarev and Derlet [11].

The paper is organized as follows. First, we describe the fitting procedure of this new potential and the total-energy calculations carried out for extending the database. Then various bulk properties are compared, including phonon dispersions and the Bain path. The next section addresses melting properties and calculations of Gibbs free energies for bcc and fcc iron. Finally, point defect properties will be discussed before the paper is concluded.

2. Development of a bond-order potential for bcc and fcc iron

2.1. Bond-order formalism

The functional form of the potential is summarized briefly by the following equations. The total energy is written as a sum over individual bond energies:

$$E = \sum_{i<j} f_{ij}^c(r_{ij}) \left[V_{ij}^R(r_{ij}) - \frac{b_{ij} + b_{ji}}{2} V_{ij}^A(r_{ij}) \right]. \tag{1}$$

The pair-like repulsive and attractive terms are taken as Morse-like pair potentials:

$$
\begin{aligned}
V^R(r) &= \frac{D_0}{S-1} \exp\left(-\beta\sqrt{2S}(r - r_0)\right), \\
V^A(r) &= \frac{SD_0}{S-1} \exp\left(-\beta\sqrt{2/S}(r - r_0)\right).
\end{aligned}
\tag{2}
$$

Here, S is an adjustable parameter, while D_0 denotes the dimer bond energy and r_0 the dimer bond length. The parameter β can be determined from the ground-state oscillation frequency of the dimer. The interaction range is determined by the cut-off function:

$$
f^c(r) =
\begin{cases}
1, & r \leqslant R - D, \\
\dfrac{1}{2} - \dfrac{1}{2} \sin\left(\dfrac{\pi}{2}(r - R)/D\right), & |R - r| \leqslant D, \\
0, & r \geqslant R + D
\end{cases}
\tag{3}
$$

where R and D are adjustable parameters. Three-body contributions and angularity enter the energy function via the bond-order parameter b_{ij}:

$$b_{ij} = (1 + \chi_{ij})^{-\frac{1}{2}}, \tag{4}$$

$$\chi_{ij} = \sum_{k \neq i,j} f_{ik}^c(r_{ik}) g_{ik}(\theta_{ijk}) \exp[2\mu_{ik}(r_{ij} - r_{ik})]. \tag{5}$$

The indices monitor the type-dependence of the parameters, which is important for describing compound systems. The angular dependence is described by

$$g(\theta) = \gamma \left(1 + \frac{c^2}{d^2} - \frac{c^2}{d^2 + [h + \cos\theta]^2} \right), \tag{6}$$

as originally proposed for sp-valent materials. By carefully adjusting the shape and minimum position, this functional form can also be applied for d transition metals [16, 17].

2.2. General fitting procedure

The general fitting methodology employed in the present work has already been described in detail before [16, 18, 17]. In short, to achieve a high transferability, the aim is to match the properties of the potential with an extensive database of values obtained from experiment and first-principles calculations. The complete set of reference data is divided into a fitting and a testing database [19, 20]. The fitting database encompasses structural properties like bond lengths, cohesive energies and elastic constants of structures covering the coordination range from the dimer up to the 12-fold coordinated close-packed fcc and hcp (hexagonal close-packed) structures. Starting from an initial guess, the potential parameters are optimized by adjusting the properties predicted by the potential to the values contained in the fitting database using a conjugate gradient least-squares minimization algorithm as implemented in the program PONTIFIX [21]. Subsequently, the quality of a parameter set, which has been identified as a good fit in this first step, is evaluated by comparing to the testing database. This database comprises

data on point defects like vacancies and interstitial formation energies, and two-dimensional defects such as surface and interface energies. Furthermore, thermal properties like the melting temperature and transitions between solid phases are also included. This procedure allows one to identify regions of parameter space where the potential shows a high transferability. Promising parameter sets can be used as a new starting point in the minimization algorithm. In iterating the fitting and testing steps, one eventually proceeds towards a parameterization that shows an overall satisfactory behaviour regarding the complete set of reference data.

2.3. Total-energy calculations

As described above, the transferability of the bond-order potential developed in this work crucially depends on an extensive fitting database covering a variety of differently coordinated structures. The experimental data available in literature are naturally constricted to phases that are accessible in experiments, like the ground-state bcc phase or the high-temperature fcc phase. For structures that do not appear in the phase diagram, density functional theory (DFT) calculations are carried out in order to fill the fitting database with the required properties.

The DFT calculations were performed using the Vienna *ab initio* simulation package VASP [22] employing the projector-augmented wave (PAW) method [23, 24]. The generalized gradient approximation (GGA) was used in the parameterization by Perdew and Wang (PW91) [25]. The plane-wave cut-off energy was set to 348.3 eV. The number of k-points in the irreducible Brillouin zone was chosen to guarantee a convergence of the total energy better than 1 meV/atom. Typical values are 220 k-points for the bcc and fcc structures.

Total energies have been calculated for Fe in the fcc, hcp, bcc, sc (simple cubic) and diamond structures. For each structure, the minimum energy, lattice constant, bulk modulus and pressure derivative of the bulk modulus were determined by fitting the energy–volume data to the Birch–Murnaghan equation of state [26]. For the hcp structure, the c/a ratio was identified by calculating energy–volume curves for different fixed c/a ratios and subsequently fitting a second-order polynomial to the energy minima. The results of the calculations are summarized in table 2.

For identifying the magnetic ground state of a structure, non-spin-polarized (non-magnetic, NM) as well as spin-polarized calculations with ferromagnetic (FM) and anti-ferromagnetic (AFM) alignment of the atomic spins were performed. The magnetic ground states are found to be NM for the diamond structure, FM for simple cubic, FM for bcc, AFM for fcc and NM for hcp. As shown in figure 1, the calculations furthermore reveal the existence of two FM states in fcc Fe, namely a high-spin, high-volume (HS) and a low-spin, low-volume (LS) state separated from the AFM state by 45 meV and 29 meV, respectively. The results on bcc, fcc and hcp Fe are in qualitative agreement with *ab initio* calculations from Entel *et al* [27, 28]. Experimental evidence for the AFM ground state of γ-Fe and the existence of the FM HS state is summarized in [29]. The energy difference between FM bcc Fe and AFM fcc Fe calculated by this method is 0.11 eV/atom.

For bcc and fcc Fe, the complete set of second-order elastic constants has been calculated. For this purpose, the deformation energy of the system was analysed in response to different deformation modes (see table 2). The GGA calculations provide an overall good description of the elastic properties of bcc iron, with a bulk modulus being however 12% larger than the reference value of 169 GPa and a somewhat too low c_{44} elastic constant. The significance of the experimentally determined elastic constants of γ-iron for comparison with the results from DFT calculations is only limited. Since the experimental values were obtained at 1428 K, a softening of the elastic constants with respect to the 0 K calculations can be expected. A deviation of the DFT results towards higher values is therefore reasonable. Furthermore, in agreement with

4
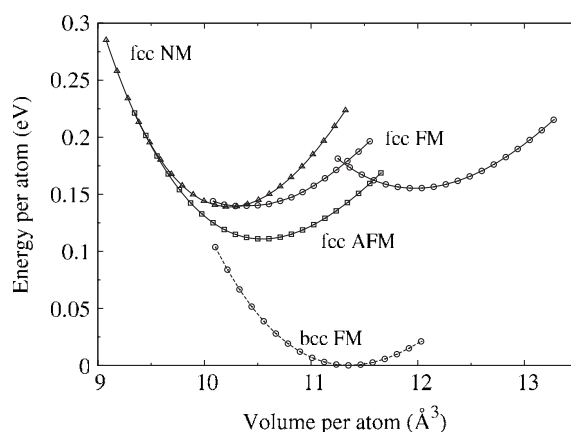
Figure 1. Comparison of energy–volume curves at 0 K for FM bcc Fe and fcc Fe in different magnetic states as obtained from DFT calculations described in this work. Energies are relative to the FM bcc ground state.

the ground state of γ-iron, an anti-ferromagnetic alignment of spins was assumed in the DFT calculations. At the temperature of the experimental measurement, the magnetic ordering is, however, not preserved and its influence on the elastic constants cannot be assessed.

The DFT data represent a complement to the available experimental data in the fitting database. However, this introduces the problem that structural properties like the bond lengths obtained from DFT calculations can deviate from experimental values simultaneously used in the fitting database. In order to obtain a consistent input data set, all atomic volumes obtained by DFT were scaled by a factor 1.03 that matches the volume of the bcc ground state to the experimental volume.

2.4. Fitting of the Fe potential

For the sake of computational efficiency, it is generally desirable to keep the cut-off radius as small as possible, reducing it to nearest-neighbour interactions only. However, the difference in bond length between the nearest and second-nearest neighbours in the bcc structure is very small, and positioning the cut-off function between the two distances can lead to unpredictable cut-off effects. The cut-off radius of the ABOP was therefore chosen in a way that second-nearest neighbours are included for the bcc structure, but are excluded for the fcc structure. (This approach has previously proven useful for describing tungsten [17].)

One quantity that proved to be decisive for the performance of the potential is the parameter h determining the position of the minimum in the angular function $g(\theta)$ (see (6)). Atomic configurations exhibiting angles close to this minimum possess a higher bond order than configurations with angles lying outside the minimum. Careful selection of the range of h therefore easily allows one to energetically favour the bcc structure over the close-packed fcc and hcp structures. As shown in figure 2, the dominating nearest-neighbour angles on a bcc lattice are 70.5° and 107.5°, which appear in figure 2 at positions $+1/3$ and $-1/3$. In contrast, the fcc lattice exhibits angles of 60°, 90° and 120°, corresponding to positions $1/2$, 0 and $-1/2$. A selection of h with $|h|$ in the vicinity of $1/3$ therefore allows one to create potentials where the bcc structure has a lower energy than the close-packed structures.

However, positioning the minimum of $g(\theta)$ exactly on or too close to an angle appearing in a structure often deteriorates the elastic properties. In this case, the fitting routine is prone to
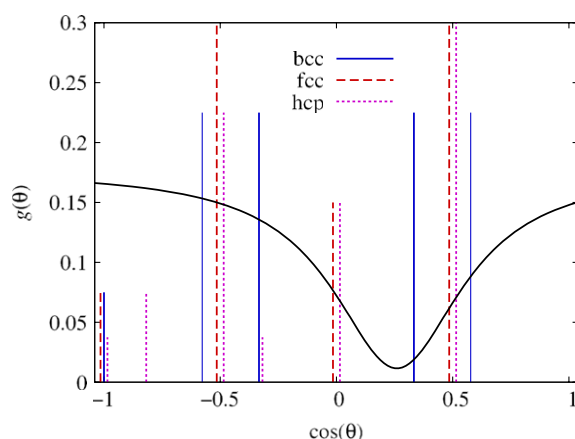
Figure 2. Angular function $g(\theta)$ of the Fe potential. Angles appearing in different structures are indicated by vertical lines. The height of a line is proportional to the weight of the angle in the respective structure. The angles are shifted slightly so that structures having identical angles can be distinguished.

the risk of stabilizing the structure by a minimum in the energy landscape arising solely from the presence of the selected angle, which leads to large restoring forces when moving the atoms away from their equilibrium positions by shear deformations. Poor elastic constants (a too high c_{44}) are also found for $|h| \geqslant 1/3$. These considerations restrict the range of $|h|$ to values close to, but lower than, 0.3.

Changing the sign of the parameter h alters the static properties of the bcc phase only slightly, since, apart from the 180° angle, the angles appearing in the bcc structure are symmetrically distributed around $\cos(\theta) = 0$. Parameter sets with a positive h around 0.3 show, however, unrealistically low melting temperatures at approximately 1000 K. For this reason, the parameter h has to be restricted to negative values.

Another restriction applies to the parameter 2μ. During the fitting procedure, it was found that the fcc Fe phase becomes thermally unstable for $2\mu > 0$. It turned out that although the fcc structure is a local minimum in the potential energy landscape, the fcc phase spontaneously transforms into a twinned bcc structure at non-zero temperatures sometimes as low as 200 K. In contrast, the thermal stability of the fcc Fe phase is maintained with parameter sets having very low values for 2μ. This parameter has therefore been restricted zero.

During the fitting process, incompatibilities between two desired properties can appear, i.e. fitting exactly to one property results in a bad performance of the potential for the other property. In some cases, this problem can be circumvented by restarting the fitting process in another region of parameter space. However, for the Fe potential an incompatibility between the correct dimer bond length and realistically high surface energies could not be resolved. Fixing the dimer bond length at the experimental value of 2.0 Å results in very low surface energies, a finding that holds true for the entire range of parameter space sampled during the fitting process. A trade off between accurate dimer properties and sufficiently high surface energies therefore has to be accepted. The final parameterization of the Fe potential exhibits a 15% too high dimer binding length of 2.29 Å but in turn yields acceptable surface energies.

An essential feature of the iron phase diagram is the α–γ transition. A correct description of this transition in classical molecular dynamics simulations is only possible if the missing contributions of the magnetic entropy are accounted for. By following the method described
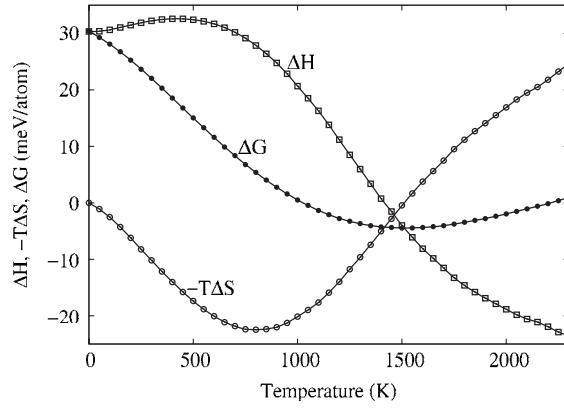
Figure 3. Enthalpy and entropy contributions to the Gibbs free energy difference $\Delta G = G(\text{fcc}) - G(\text{bcc})$ between the fcc and bcc phases of the iron potential developed in this work.

Table 1. Final parameter set of the analytic bond-order potential for iron.

Parameter	Value
D_0 (eV)	1.5
r_0 (Å)	2.29
β (Å^{-1})	1.4
S	2.069 3109
γ	0.011 5751
c	1.289 8716
d	0.341 3219
h	-0.26
2μ (Å^{-1})	0.0
R (Å)	3.15
D (Å)	0.2

in the appendix, the temperature dependence of the Gibbs free energy difference $\Delta G = G(\text{fcc}) - G(\text{bcc})$ has been calculated for different trial parameterizations. The general shape of the ΔG curve was found to be universal for the region of parameter space sampled. It is plotted as an example for the final parameterization of the ABOP in figure 3, together with the contributions from enthalpy and entropy. After an initial decrease, ΔG reaches a minimum at intermediate temperatures and increases again up to the melting point. Although, in general, the ΔG curve does not give rise to a bcc–fcc phase transition for an arbitrary parameterization, this general shape suggests the following procedure for fitting the potential to the $\alpha-\gamma$ transition. The missing contributions of the magnetic entropy can be compensated purely by vibronic contributions if the fcc–bcc energy difference ΔE is regarded as an adjustable parameter allowing one to shift the ΔG curve until a phase transition is located in the correct temperature regime. The potential is then regarded as an effective energy function that best describes the behaviour of the real iron system.

In practice, the fitting procedure proved to be more complex, since a change in ΔE does not only shift the ΔG curve, but the new parameter set can also lead to a change in the slope of ΔG over T. A trial and error process therefore had to be adopted. The final best-fit parameter set developed by this method is given in table 1.

Table 2. Comparison of structural and cohesive properties of Fe in various phases from calculation and experiment. Errors are given in round brackets. Values in square brackets are rescaled to the experimental atomic volume of bcc Fe. For the DFT calculations, the parameters are given for the lowest-energy magnetic configuration, as indicated. r_b: dimer bond distance (Å), E_b: dimer binding energy (eV/atom), ω_0: dimer vibration frequency (cm^{-1}), V: equilibrium volume (Å^3/atom), a_0: lattice constant (Å), c/a: axial ratio, E_c: cohesive energy (eV/atom), ΔE: energy difference (eV/atom) to ground state (FM bcc), ΔE_{Bain}: energy barrier (meV/atom) between fcc and bcc phase along Bain path, B, B': bulk modulus (GPa) and its pressure derivative, c_{ij}: elastic constants (GPa).

	PAW GGA–DFT This work	Literature Experiment	Literature Theory	Simonelli Ref. [6]	Ackland Ref. [7]	Mendelev Ref. [10]	Dudarev Ref. [11]	ABOP
Dimer								
r_b		2.02[a]	2.01[e]	2.11	2.35	2.19	2.24	2.29
E_b		1.04[b], 1.14[c]	1.65[e]	4.12	2.86	3.01	4.44	1.50
ω_0		299[d]	397[e]	350(10)	293	305(5)	510(10)	239
Diamond ($Fd\bar{3}m$), non-magnetic								
V	14.31 [14.74]			21.70	23.46	19.82	24.17	21.45
a_0	4.856 [4.904]			5.578	5.726	5.413	5.783	5.557
ΔE	1.17			1.43	1.69	1.42	1.48	2.13
Simple cubic ($Pm\bar{3}m$), ferromagnetic								
V	13.26 [13.66]			13.42	12.79	11.27	10.89	14.13
a_0	2.367 [2.390]			2.376	2.339	2.24	2.216	2.417
ΔE	0.75			0.80	1.08	0.71	0.81	1.15
Body-centred cubic ($Im\bar{3}m$), ferromagnetic								
V	11.36 [11.70]	11.70[f]		11.78	11.77	11.64	11.78	11.70
a_0	2.832 [2.860]	2.860[f]		2.866	2.866	2.855	2.866	2.860
E_c	−4.28[g]	−4.28[h]		−4.280	−4.316	−4.127	−4.316	−4.280
B	189	169[i]		178	178	178	173	169
B'	5.1			4.5	4.8	1.5	−1	4.6
c_{11}	277	226[i]		242	243	243	243	225
c_{12}	147	140[i]		146	145	145	138	142
c_{44}	96	116[i]		112	116	116	122	126
Face-centred cubic ($Fm\bar{3}m$), anti-ferromagnetic								
V	10.55 [10.87]	11.30[f]		12.07	12.45	12.24	11.74	11.77
a_0	3.482 [3.516]	3.562[f]		3.641	3.680	3.658	3.608	3.611
ΔE	0.11		0.06[j]	0.026	0.054	0.121	0.086	0.030
ΔE_{Bain}			45[k]	4	8	0.7	12	36
B	199	133[l]		140	144	49	130	164
B'	5.5			5.9	1.0	11	4.9	4.6
c_{11}	309	154[l]		160	187	67	175	204
c_{12}	152	122[l]		130	121	40	108	144
c_{44}	201	77[l]		101	98	10	99	101
Hexagonal close-packed ($P6_3/mmc$), non-magnetic								
V	10.18 [10.48]			12.07	12.43	12.24	11.75	11.77
a_0	2.459 [2.484]			2.574	2.600	2.607	2.552	2.555
c/a	1.58			1.633	1.633	1.595	1.633	1.63
ΔE	0.06			0.026	0.054	0.117	0.086	0.027

[a] Reference [30]. [b] Reference [31]. [c] Reference [32]. [d] Reference [33].
[e] Reference [34]. [f] Reference [29] Lattice constant extrapolated to 0 K. [g] Value taken from experimental data.
[h] Reference [35]. [i] Reference [36]. [j] Reference [37].
[k] Reference [38]. [l] Reference [39] Phonon dispersion measurement at 1428 K.

3. Comparison of the ABOP with existing EAM potentials

In the following, the predictions of the ABOP for an extensive set of properties are compared to reference values from experiment and simulation. The performance of the ABOP is discussed in comparison with the EAM potentials by Simonelli [6], Ackland [7], Mendelev [10] and Dudarev [11].

3.1. Dimer and bulk properties

The dimer properties, the cohesive energies and structural parameters of iron in the diamond, sc, bcc, fcc and hcp structures, as well as the elastic constants of the bcc and fcc structures as predicted by the ABOP and EAM potentials, are compared in table 2 with reference data from literature and total-energy calculations.

All potentials predict a dimer binding length higher than the experimental value of $r_b = 2.0$ Å [30]. The values range from 2.11 Å for the Simonelli potential up to 2.35 Å for the Ackland potential. The ABOP also gives a rather high r_b of 2.29 Å. As mentioned in the description of the fitting process, this deviation is a necessity for obtaining acceptable surface energies with the ABOP. With 1.50 eV, the dimer binding energy is well reproduced by the ABOP: the reference values scatter between 1.04 and 1.65 eV [31, 34]. In contrast, all EAM parameterizations systematically overestimate the dimer binding energy by at least a factor 2.

The ABOP was fitted exactly to the experimental reference data on the cohesive energy, lattice constant and elastic constants of the ground-state bcc structure. These parameters are therefore reproduced with good accuracy; only the elastic constant c_{44} is slightly too high. Deviations of the EAM potentials from this basic experimental data occur for several reasons. No reference data for the cohesive energy of bcc iron are given in the paper by Ackland *et al*; instead, the reported value of -4.316 eV/atom is the cohesive energy obtained from their potential [7]. This value has then been used as a reference in the works of Dudarev *et al* [11] and Mendelev *et al* [10]. For achieving a better agreement of other parameters with experiment, the latter potential was fitted with only little weight on the cohesive energy, explaining the value of -4.127 eV/atom. The deviations of the elastic constants of the EAM potentials from the experimental values given in table 2 mainly arise from the utilization of different reference values. The deviations therefore give no indication of the quality of the potentials; they rather deliver insight on the scattering of the experimental data. Fitting the energy–volume curve of bcc Fe obtained from the Dudarev potential to the Birch–Murnaghan equation of state reveals, however, a negative pressure derivative of the bulk modulus, which implies that an expansion of the bcc crystal from the equilibrium volume requires a higher energy than a compression. As shown in section 3.3, the Dudarev potential consequentially possesses a negative expansion coefficient.

In the case of γ-iron, all potentials produce too high equilibrium atomic volumes. The ABOP (11.77 Å^3) and the Dudarev (11.74 Å^3) potential are closest to the reference value of 11.30 Å^3. Also, only in the case of the Dudarev potential, the fcc structure has an at least slightly lower atomic volume than the bcc structure. In contrast, the Ackland (12.45 Å^3) and Mendelev (12.24 Å^3) potentials severely overestimate the atomic volumes. Here it is to be said that Mendelev *et al* used a reference value of 3.6583 Å for the lattice constant of fcc iron at 0 K, obtained from first-principles calculations performed as a part of their work in [10]. This value is, however, already larger than experimental results for the lattice constant of γ-iron at room temperature (3.569 Å; see [29] and references therein).

The elastic constants of γ-iron predicted by the ABOP are 20%–30% higher than the reference values extracted from phonon dispersion measurements at 1428 K [39]. On the other

hand, the elastic constants remain markedly below the values obtained from DFT calculations. Considering the expected softening of the crystal at elevated temperatures, and taking into account that GGA–DFT calculations tend to overestimate the elastic constants of iron, it is reasonable to obtain elastic constants that lie between the high-temperature experimental values and the *ab initio* data. Apart from the Mendelev potential, the EAM potentials also yield fcc elastic constants of roughly the same magnitude. The elastic constants of the Mendelev potential are undoubtedly too low. With c_{44} being only 10 GPa, the fcc structure is close to being mechanically unstable.

The structural energy difference ΔE between fcc and bcc iron predicted by the potentials ranges from 0.026 eV/atom (Simonelli) and 0.030 eV/atom (ABOP) up to 0.121 eV/atom for the Mendelev potential. During the fitting process of the potentials, different strategies for determining ΔE have been applied. Consequentially, the significance of the final value for ΔE varies between the potentials. In the Simonelli and Ackland potentials, ΔE was not explicitly considered but merely served to render the bcc phase the ground-state structure, i.e. care was taken that ΔE assumed a reasonably positive value. On the other hand, in the case of the Mendelev and Dudarev potentials, ΔE has been fitted to *ab initio* calculations, eventually leading to markedly higher values[1]. Finally, as discussed in section 2.4, during the fitting process of the ABOP, ΔE is considered as an adjustable parameter providing the necessary flexibility to the effective energy function for reproducing the bcc to fcc phase transition in real iron. In consequence, the final value of $\Delta E = 0.03$ eV/atom is significantly lower than the reference value from DFT calculations (0.11 eV/atom), as well as the value estimated by a thermodynamic assessment of the Fe phase diagram (0.06 eV/atom) [37].

For the hcp structure, all potentials produce the same atomic volume as for the fcc structure. This represents a deviation from the total-energy calculations, which yield an atomic volume that is smaller than in the case of fcc. Apart from the Dudarev potential, the atomic volume of the hcp structure is furthermore higher than the atomic volume of the bcc structure. Therefore, the hcp structure is not correctly reproduced as the high-pressure equilibrium phase at 0 K. Instead, a negative pressure is required for realizing a transition from the bcc to the hcp phase. Also, the DFT calculations predict that, at 0 K, the hcp structure is more stable than the fcc structure. Only the ABOP and the Mendelev potential yield cohesive energies for the fcc and hcp phases that are in consistency with this finding. For the remaining potentials, the cohesive energies for the fcc and hcp structures are identical.

At lower coordination, all potentials perform reasonably well in reproducing the cohesive energy and lattice constant of the sc structure. In contrast, for the diamond structure, all potentials significantly overestimate the lattice constant on one hand but underestimate the cohesive energy on the other hand. As previously discussed for the fcc and bcc structures, magnetic effects have an important influence on the cohesive energy and bond length. Considering the multiple changes of magnetic ground state in the DFT data when proceeding from high coordination up to the diamond structure, it is understandable that the potentials cannot grasp all the resulting effects and the deviations at low coordination are acceptable.

3.2. Bain path

As shown in figure 4, the bcc lattice can be regarded as a tetragonally distorted fcc lattice and vice versa. A possible transformation path from the bcc to the fcc structure is therefore the

---

[1] The energy difference between the fcc and bcc structures of the Dudarev Fe potential calculated in this work and listed in table 2 differs from the value given in table 1 of [11]. It is, however, consistent with the energy difference extracted from figure 4 of [11]. It therefore appears that table 1 of [11] does not contain the properties of the final parameterization of the Fe EAM potential.
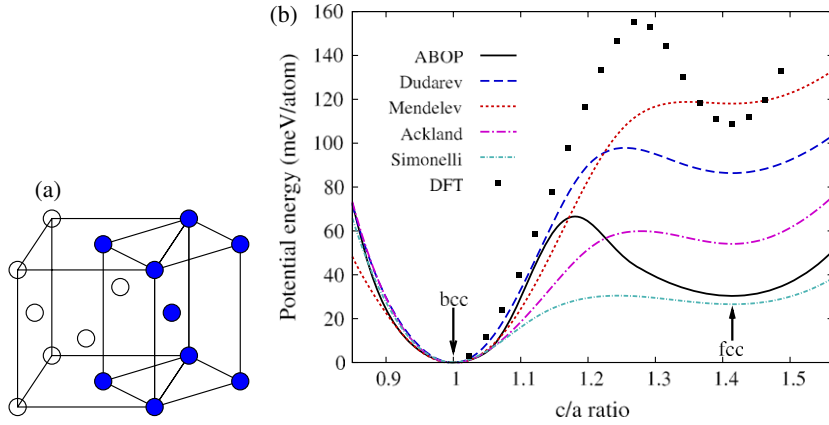
Figure 4. (a) Geometrical correlation between the fcc and bcc unit cells. The fcc structure (open circles) can be regarded as a tetragonally distorted bcc structure (filled circles) with an axial ratio of $c/a = \sqrt{2}$. (b) Fe Bain path. The energy scale is relative to the ground-state bcc structure of the respective potentials. Data from DFT calculations are taken from [38].

uniaxial expansion of the bcc unit cell along a $\langle 100 \rangle$ direction, which is also known as the Bain path. In figure 4, the energetics of this transformation predicted by the analytic potentials is compared with results from GGA–DFT calculations on ferromagnetic iron taken from [38]. It visualizes the previously discussed energy differences between the fcc and bcc structures predicted by the analytic potentials. Furthermore, the energy barrier ΔE_{Bain} that has to be overcome for a transition from fcc to bcc along the Bain path can be extracted. The value for ΔE_{Bain} estimated by the DFT calculations is 45 meV/atom. With $\Delta E_{\text{Bain}} = 36$ meV/atom, the ABOP is closest to this reference value. In contrast, all EAM potentials predict significantly lower transition barriers. The smallest barrier is given by the Mendelev potential, where ΔE_{Bain} is less than 1 meV/atom. In this case, the transition requires almost no activation, making the fcc phase extremely unstable.

An apparent difference in the Bain paths plotted in figure 4 is the much higher curvature of the local fcc minimum obtained from DFT calculations as compared to the ABOP. For small tetragonal distortions of a cubic lattice, the curvature of the energy–strain curve is proportional to the elastic constant C', with $C' = (c_{11} - c_{12})/2$. GGA–DFT calculations predict a much higher C' than is justifiable by the experimental data on elastic constants of γ-iron (see table 2). In contrast, C' obtained from the ABOP is in reasonable agreement with the experimental data. The low curvature of the fcc minimum of the ABOP therefore appears to be more realistic. For the same reason, obtaining a somewhat smaller barrier ΔE_{Bain} than the GGA–DFT reference value also seems to be reasonable.

3.3. Melting properties and thermal expansion

For determining the melting point of Fe at zero pressure, molecular-dynamics simulations of a solid–liquid interface in the $N, P = 0, T$ ensemble have been performed. For different temperatures around the expected melting point, the position of the solid–liquid interface was monitored and the actual melting temperature was found for zero velocity of the interface, i.e. when the volume fractions of the solid and liquid phases remain constant over the simulation time of 0.5 ns. The melting point for the ABOP estimated by this method is 2270(20) K, which is distinctly higher than the experimental value of 1811 K [4]. The Ackland and Dudarev

potentials give a similar overestimation of the melting point; only the Simonelli and Mendelev potentials produce melting temperatures of the correct magnitude.

The room-temperature (RT) linear expansion coefficient α_L of bcc iron predicted by the Simonelli, Ackland and Mendelev EAM potentials is lower than, but reasonably close to, the experimental value of 11.8×10^{-6} K^{-1} [36]. In accordance with a negative pressure derivative of the bulk modulus (see table 2), the Dudarev potential possesses a negative linear thermal expansion coefficient of -6×10^{-6} K^{-1}. The ABOP features a rather low α_L of only 2.1×10^{-6} K^{-1}. This shortcoming of the ABOP is a compromise that has to be accepted for fitting the potential to the bcc to fcc phase transition. Preliminary parameterizations of the Fe potential having a higher fcc to bcc energy difference ΔE than the final potential, and consequently not showing a transition between the two phases, displayed expansion coefficients closer to the experimental value. A reduction of ΔE, while remaining in the same region of parameter space, is then observed to be accompanied by a lowering of α_L.

The expansion coefficient for γ-iron has been evaluated at RT and 1500 K, the last temperature lying within the stability region of the fcc phase. Compared to the experimental values, the potentials underestimate the thermal expansion by more than a factor of 2. Interestingly, in qualitative agreement with experiment [29], the ABOP shows a smaller expansion coefficient for γ-iron at high temperatures than at room temperature.

A deficiency of the potentials by Dudarev and Mendelev in describing fcc iron is revealed when simulating the fcc structure at finite temperatures. At temperatures as low as 200 K, the fcc structure does not remain stable. Instead, a transition to a twinned bcc structure is observed after just a few picoseconds. In consequence, thermal properties of the fcc phase cannot be evaluated for these potentials. In general, such a behaviour would not present a failure of the potentials, if restricted to the low-temperature regime where the bcc phase is the thermodynamically stable phase in the real iron system. The instability of the fcc phase remains, however, intact up to the respective melting points of the potentials. In the case of the Mendelev potential, this instability can be explained both by the low elastic constants of the fcc structure (see table 2) and by the almost non-existent barrier between the fcc and bcc phases when following the Bain path (see figure 4). Instead, the Dudarev potential possesses a distinctive barrier of 12 meV in the Bain path. This barrier is larger than in the case of the Simonelli and Ackland potentials, both showing a thermally stable fcc structure. The Bain path does therefore not provide an explanation for the thermal instability of the fcc structure in the Dudarev potential. Also, the elastic constants of the fcc phase are reasonably high and do not give an indication for an instability. The energy function of the Dudarev potential therefore has to provide another artificially low energy path connecting the fcc phase with the bcc phase.

3.4. BCC to FCC phase transition

Whether or not the analytic iron potentials reproduce the bcc α-iron to fcc γ-iron phase transition has been examined by calculating the fcc to bcc Gibbs free energy difference up to the melting point of the respective potentials. As described in the appendix, the Gibbs free energies of both phases at a temperature T_0 can be determined by the coupling-parameter method [52]. The temperature dependence of the Gibbs free energy is then obtained by integrating the Gibbs–Helmholtz equation.

The lack of a thermally stable fcc phase makes these calculations redundant for both the Mendelev and Dudarev potentials. For the remaining potentials, the fcc to bcc Gibbs free energy difference ΔG is plotted in figure 5. Starting from the respective 0 K structural energy difference ΔE, all potentials feature an initial decrease of ΔG with increasing temperature.
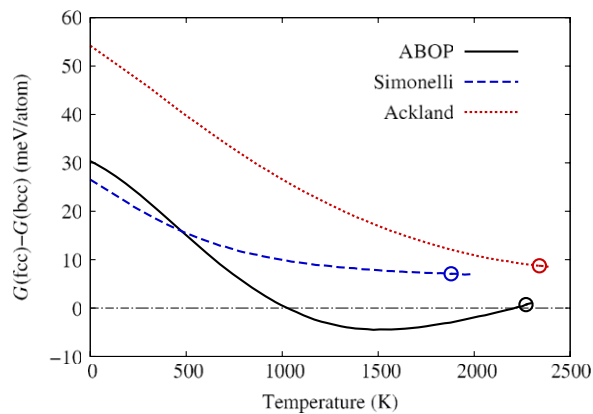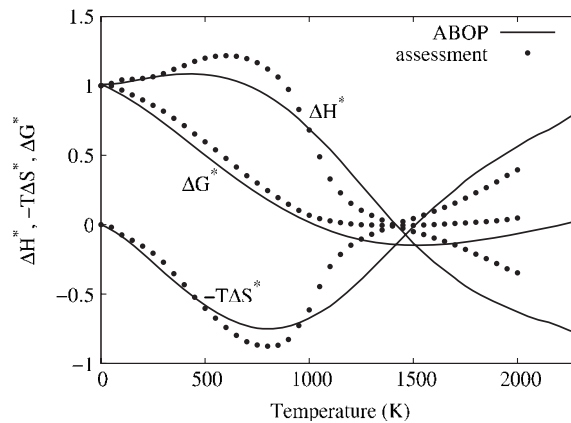
Figure 5. Gibbs free energy difference between the Fe fcc and bcc phases, as obtained from different interatomic potentials. Open circles indicate the melting points of the respective potentials.

However, a bcc to fcc phase transition is absent for both the Simonelli and the Ackland EAM potentials, with ΔG remaining positive up to the melting temperature.

In the case of the Ackland potential, Gibbs free energy calculations have already been published by Lopasso and co-workers in [53]. The same methods for calculating free energies as in the present work were used, only with the coupling-parameter method implemented in a MD instead of a Monte Carlo (MC) simulation. Their results slightly differ from the calculations performed in this work: the calculations of Lopasso *et al* do predict the presence of a bcc to fcc transition at 2343 K, located just below the somewhat higher melting temperature of 2396 K found by their method. However, applying their increased melting temperature to the ΔG curve in figure 5 would still not give rise to a thermodynamic stability of fcc iron from our calculations. According to the Gibbs free energy calculations performed in this work, the Ackland potential gives a ΔG that is still larger than 8 meV/atom at 2400 K. As described in the appendix, by double checking the results, any presence of systematic errors in the implementation of the coupling-parameter method or the integration of the Gibbs–Helmholtz equation in this work can be ruled out. In contrast, a possible source for the discrepancies between both calculations can be finite-size effects. In [53], the simulation cells consist of 686 atoms for the bcc structure and 500 atoms for the fcc structure. The simulations in the present work are performed with 1024 atoms for the bcc structure and 1008 atoms for the fcc structure. However, it should be noted that an analysis of finite-size effects performed as part of this work gives a difference of less than 1 meV/atom for ΔG at 2100 K when applying both sets of cell sizes. Finite-size effects might, however, be of a different magnitude in an MD implementation of the coupling-parameter method, as done in [53].

The same authors also recently published calculations of Gibbs free energies for the Simonelli EAM potential [54]. Here, they find in agreement with our results that the bcc phase remains the stable solid phase up to the melting point. The melting point obtained from their Gibbs free energy calculations of 2103 K is, however, significantly higher than the value found by the solid–liquid interface method of 1910(20) K. Also, their finding that the fcc structure is thermally unstable in simulations above room temperature (identical to the thermal instability of fcc iron found for the Mendelev and Dudarev potentials) cannot be confirmed from the simulations of the present work. The sources for these discrepancies remain unclear.

Figure 6. Evolution of reduced enthalpy, entropy and Gibbs free energy difference between fcc and bcc iron over temperature, as obtained from the ABOP and from a thermodynamic assessment of the Fe phase diagram [37]. For better qualitative comparison, all energies are scaled by the reciprocal 0 K structural energy difference between the fcc and bcc phases.

As shown in figure 5, only the ABOP succeeds in reproducing the alternating phase stability of bcc and fcc iron. Here, the bcc to fcc phase transition is located at 1030 K, which is in good agreement with the real transition temperature of 1184 K [4]. A remarkable feature of the ABOP is furthermore the rise of ΔG at temperatures above 1500 K. This increase eventually leads to a stabilization of the bcc over the fcc phase again at 2210 K, just before the potential reaches its melting point at 2270 K. This behaviour is consistent with the γ-iron to δ-iron phase transition in the real iron system, located however at 1665 K [4].

The contributions of entropy and enthalpy to the temperature evolution of ΔG are plotted in figure 6, in comparison with data obtained from a thermodynamic assessment of the iron phase diagram [37]. The 0 K structural energy difference between fcc and bcc iron of $\Delta E = 60$ meV/atom obtained by the latter method is twice as high as the value from the ABOP. For a better visualization of the general trends obtained from both methods, all energies in figure 6 are therefore scaled by a factor $1/\Delta E$. For the absolute values, see figure 3 and [37]. The qualitative agreement between both methods is remarkable. The ABOP not only reproduces the phase transitions in itself, but also the correct ratios of the entropy and enthalpy contributions to ΔG. After a slight increase at lower temperatures, the enthalpy difference ΔH decreases up to the melting point, eventually becoming negative. At the α to γ transition temperature, however, ΔH preserves a positive value. Instead, it is the excess of entropy of the fcc phase that accounts for the phase transition. After an initial decrease, the entropy contribution $-T\Delta S$ reaches a minimum around 800 K and finally assumes positive values at temperatures above 1500 K. Again, it is this contribution to ΔG that overcompensates the negative ΔH, leading to the renewed stability of the bcc phase in the temperature regime just below the melting point.

The excellent performance of the ABOP in reproducing the alternating relative thermodynamic stabilities of the bcc and fcc phases shows that analytic interatomic potentials can be successfully applied for describing complicated systems. Care must, however, be taken to identify shortcomings of the potential function in describing all contributions to energy and entropy present in the real system. As is shown in the present case of magnetic iron, a compensation of missing contributions is possible by regarding the potential as an effective energy function, which requires a consistent scaling of structural energy differences.
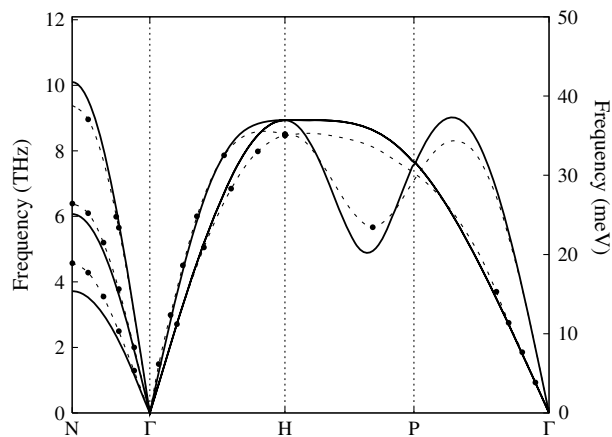
Figure 7. Phonon dispersion of bcc α-Fe as calculated from the ABOP potential developed in this work. Black dots denote experimental data points [55].

3.5. Surfaces and stacking-faults

The energies of planar defects like low-index surfaces and stacking-fault configurations obtained from the ABOP and EAM potentials are compared with reference values from experiment and theory in table 3.

The different potentials produce very similar results for the relaxed low-index surface energies of bcc, as well as fcc iron. For bcc iron, surface energies are available both from experiment [48] and theory [49]. Compared to these reference values, it is evident that the surface energies of the potentials are on average 30%–40% too small.

The unstable generalized stacking-fault energy γ^{USF} has been examined for different slip systems. The fault energies are in good overall agreement with data from first-principles calculations [50]. The lowest activation for slip is found in the $(110)[1\bar{1}1]$ system. However, all potentials overestimate the value for the respective γ^{USF}.

3.6. Phonon dispersions

The phonon dispersions for bcc as well as fcc Fe predicted by the ABOP are shown in figures 7 and 8 together with data points from experiment [39, 55]. An inspection of figure 7 reveals an excellent agreement of the bcc phonon dispersion with the reference data.

The phonon dispersion of fcc iron has been measured at 1428 K [39]. For consistency, the phonon dispersion of fcc iron of the ABOP has been calculated at the 1428 K atomic volume of 12.27 Å^3/atom. As shown in figure 8, the phonon frequencies are somewhat higher than the experimental reference data. This difference can be attributed to the fact that the phonon softening is underestimated because of the weak lattice expansion predicted by the potential.

Not shown are the phonon dispersions of the EAM potentials. In general, all EAM potentials perform well in reproducing the phonon dispersion of the bcc phase. Also, similar to the ABOP, higher phonon frequencies than in the 1428 K reference data are found for the fcc phase. The only exception is the Mendelev potential, where, in line with the low elastic constants, the phonon frequencies of the fcc phase are significantly underestimated.

Table 3. Comparison of thermal, point defect and surface properties of bcc and fcc Fe as obtained from analytic potentials with literature data. Errors are given in round brackets. Curly brackets denote values taken from the original publications deviating from our calculations. T_m: melting point (K), α_L: coefficient of linear thermal expansion (10^{-6} K^{-1}), ΔE_v^f: vacancy formation energy (eV), ΔV_v: vacancy relaxation volume (in units of atomic volume), ΔE_v^m: vacancy migration energy, ΔE_i^f: interstitial formation energy (eV), ΔV_i^f: formation volume of the lowest-energy interstitial (in units of atomic volume), ΔE_i^m: interstitial migration energy (eV), $E_{\langle uvw \rangle}^d$: threshold displacement energy in direction $\langle uvw \rangle$ (eV), E_{av}^d: threshold displacement energy averaged over all directions (eV), $\gamma_{(hkl)}$: energy of (hkl)-surface (meV Å^{-2}), $\gamma_{(hkl)[uvw]}^{USF}$: relaxed unstable stacking fault energy for $(hkl)[uvw]$ slip system (J m^{-2}).

| | Literature | | | | | | |
	Experiment	Theory	Simonelli	Ackland	Mendelev	Dudarev	ABOP
T_m	1811[a]		1910(20)	2340(20)	1760(30)	2160(20)	2270(20)
Body-centred cubic ($Im\bar{3}m$)							
α_L (RT)	11.8[b]		8.4	9.4	8.4	−6.0	2.1
ΔE_v^f	1.59–1.89[a]		1.63	1.70	1.71 {1.84}	1.86 {1.97}	1.56
ΔV_v			−0.19	−0.18	−0.23	−0.41	−0.37
ΔE_v^m	0.55[a]		0.46	0.63	0.47	0.58	0.57
$\Delta E_{i,\langle 110 \rangle}^f$		3.41[c], 3.64[d]	3.67	4.87	3.50	3.65	4.19
$\Delta E_{i,\langle 111 \rangle}^f$		4.11[c], 4.34[d]	3.54	5.01	3.99	4.24	4.59
$\Delta E_{i,\langle 100 \rangle}^f$		4.37[c], 4.64[d]	4.57	6.10	4.32	4.58	5.51
ΔV_i^f	1.1[a]		0.2	0.76	0.22	−0.57	0.37
ΔE_i^m	0.25–0.30[a]		0.03	0.04	0.18	0.15	0.17
$E_{\langle 100 \rangle}^d$	17[e], 20[f]		15[g][h]	17[g]	15[g]		15[i]
$E_{\langle 110 \rangle}^d$	>30[e], 30[f]		27[g][h]	31[g]	27[g]		23[i]
$E_{\langle 111 \rangle}^d$	20[e]		19[g][h]	35[g]	25[g]		19[i]
E_{av}^d			42.4[g][h]	44.8[g]	36.9[g]		36.7[i]
$\gamma_{(100)}$	150[j]	143[k]	102	113	111	112	104
$\gamma_{(110)}$	150[j]	142[k]	90	99	103	101	85
$\gamma_{(111)}$	150[j]	157[k]	112	125	125	125	115
$\gamma_{(211)}$	150[j]		103	114	118	116	104
$\gamma_{(010)[001]}^{USF}$		1.87[l], 1.79[m]	2.09	2.35	1.85	2.20	2.15
$\gamma_{(110)[001]}^{USF}$		1.43[l], 1.40[m]	1.76	2.22	1.75	2.05	1.93
$\gamma_{(110)[1\bar{1}1]}^{USF}$		0.59[l], 0.47[m]	0.74	0.90	0.66	0.90	0.90
Face-centred cubic ($Fm\bar{3}m$)							
α_L (RT)	24.5[n]		9.0	2.0			10.5
α_L (1500 K)	23.3[n]		10.1	6.9			7.7
ΔE_v^f	1.71[o]		1.78	1.92	1.75	1.95	1.92
ΔV_v^f			−0.11	+0.91	−0.37	−0.10	−0.26
ΔE_v^m			0.27	0.30			0.32
$\Delta E_{i,\langle 100 \rangle}^f$			3.18	3.63		3.03	3.35
$\Delta E_{i,\langle 111 \rangle}^f$			3.28	3.85		2.98	3.80
ΔV_i^f			0.38	0.10		0.56	0.58
ΔE_i^m			0.13	0.21			0.40
$\gamma_{(100)}$			94	104	98	102	103
$\gamma_{(110)}$			102	112	107	109	115
$\gamma_{(111)}$			82	88	90	90	87

[a] Reference [4]. [b] Reference [36]. [c] Reference [40]. [d] Reference [41]. [e] Reference [42]. [f] Reference [43]. [g] Reference [44]. [h] Repulsive part by Becquart *et al*, Reference [45, 46]. [i] Reference [47]. [j] Liquid surface tension measurements, Reference [48]. [k] Reference [49]. [l] Spin-polarized LDA, Reference [50]. [m] Spin-polarized GGA, Reference [50]. [n] Reference [29]. [o] Reference [51].
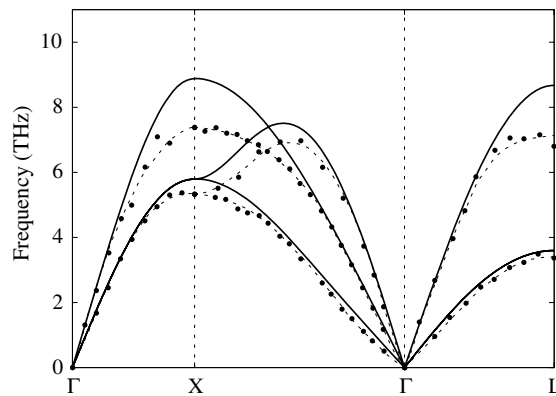
Figure 8. Phonon dispersion of fcc γ-Fe as obtained from the ABOP at the 1428 K atomic volume of 12.27 Å^3/atom. Black dots denote experimental data points measured at 1428 K [39].

3.7. Point defects

Properties of point defects in bcc and fcc iron as predicted by the analytic potentials are listed in table 3, together with reference values from the literature.

3.7.1. Static properties. *BCC α-iron.* The bcc vacancy formation energies of all potentials considered in this work lie roughly within the scattering range of the experimental data between 1.59 and 1.89 eV [4], with the ABOP (1.56 eV) marking the lower boundary and the Dudarev (1.86 eV) potential marking the upper boundary.

The energetic ordering of self-interstitial (SI) configurations represents a peculiarity of the bcc Fe system compared to other bcc transition metals [56]. In consistency with experimental findings [4], *ab initio* calculations predict the $\langle 110 \rangle$ dumbbell configuration as the most stable SI defect in bcc iron [40, 41]. Both calculations concordantly estimate the energy difference to the next stable $\langle 111 \rangle$ dumbbell configuration to be 0.7 eV. With the *ab initio* data at hand, the more recent Fe EAM potentials by Mendelev and Dudarev have been fitted to reproduce these interstitial properties [10, 11]. Both potentials yield the $\langle 110 \rangle$ as the most stable configuration with the formation energy close to the reference values. The energy difference to the $\langle 111 \rangle$ dumbbell is 0.5 and 0.6 eV, respectively. The Ackland potential also reproduces the correct ordering of interstitial configurations; the formation energies are, however, significantly higher than the *ab initio* data. Finally, the Simonelli potential falsely predicts the $\langle 111 \rangle$ dumbbell as the energetically most favourable configuration.

Regarding energetics only, the Dudarev EAM potential seems to provide a good description of SI defects. However, this potential yields negative formation volumes for all interstitial configurations considered. This finding puts into question whether this potential is able to give a physically meaningful description of the relaxation properties.

The ABOP developed in the present work reproduces the correct ordering of SI configurations. With 4.19 eV, the formation energy of the $\langle 110 \rangle$ dumbbell is somewhat higher than the reference values of 3.41 [40] or 3.64 eV [41], but still lower than the value obtained from the Ackland potential. The energy difference to the $\langle 111 \rangle$ dumbbell is 0.4 eV. For the $\langle 110 \rangle$ dumbbell, the ABOP yields an SI formation volume of 0.37 atomic volumes.

FCC γ-iron. For fcc iron, experimental data are only available for the vacancy formation energy, which has been determined by Kim and Buyers by positron annihilation
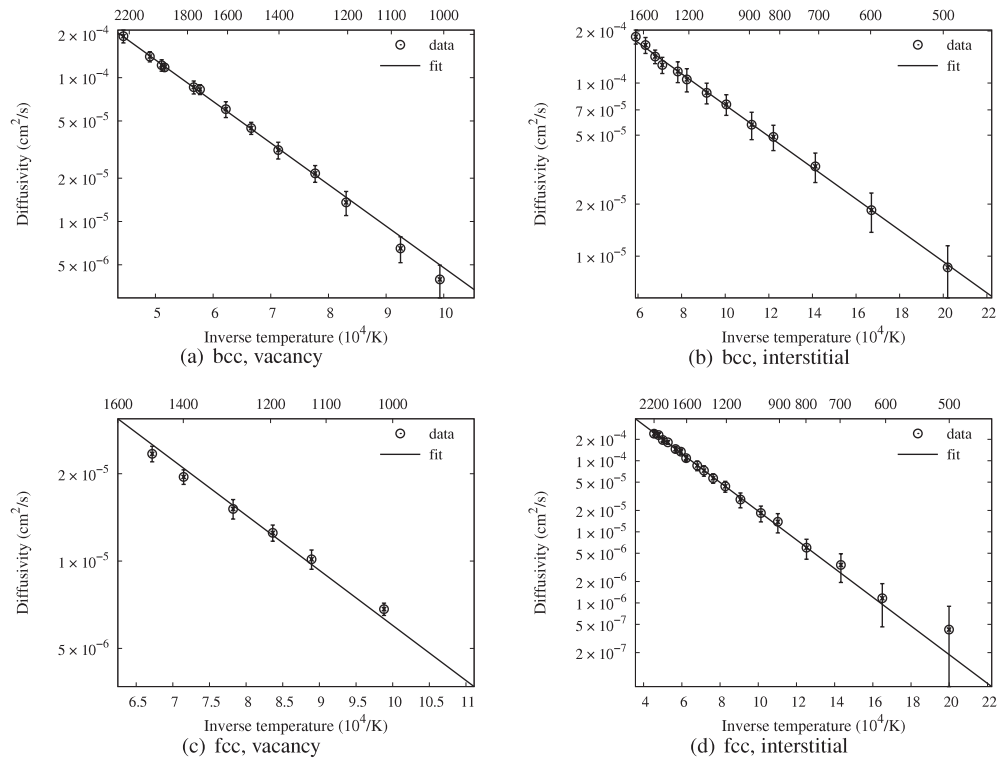
Figure 9. Temperature dependence of vacancy and interstitial diffusivities in bcc and fcc iron as predicted by the analytic bond-order potential for iron developed in this work. The simulations were carried out in the N, V, E ensemble using periodic cells containing one defect in $8 \times 8 \times 8$ or $7 \times 7 \times 7$ unit cells for bcc and fcc, respectively.

spectroscopy [51]. Their result for the formation energy is 1.71 eV. The magnitude of this value is well reproduced by all Fe potentials.

For SI defects in fcc iron, the ABOP as well as the Simonelli and Ackland potentials predict the $\langle 100 \rangle$ dumbbell as the lowest-energy configuration. In contrast, with the Dudarev potential the $\langle 111 \rangle$ dumbbell has a slightly lower energy than the $\langle 100 \rangle$ dumbbell. The SI formation energy predicted by the potentials varies between 2.98 and 3.63 eV, with the ABOP lying in the middle of this interval. For the Mendelev potential, the fcc structure does not remain stable when inserting an SI atom and no values can be given.

3.7.2. Dynamic properties. The diffusivity of point defects has been calculated using MD simulations and monitoring the mean-square displacement over an extended temperature range. The simulations were carried out in the N, V, E ensemble, because the scaling of velocities and positions by the utilization of thermostats and barostats can falsify the dynamics of the atoms. Therefore, for each temperature, the size of the simulation box was first equilibrated in an $N, P = 0, T$ ensemble calculation. Fixed at the equilibrated volume, the kinetic energy of the atoms was then equilibrated in an N, V, T run. Finally, the mean-square displacements $\langle R^2 \rangle$ were followed over a period of time τ in the N, V, E ensemble. The diffusivity D is given by the Einstein–Smoluchowski equation in three dimensions: $\langle R^2 \rangle = 6D\tau$. Migration energies have been obtained by fitting Arrhenius laws to the accumulated diffusivity data. As an example, the diffusivities of the ABOP are plotted in figure 9.

BCC α-iron. The vacancy migration energy $\Delta E_{\mathrm{v}}^{\mathrm{m}}$ in bcc Fe obtained by this method is 0.57 eV for the ABOP, in perfect agreement with the experimental value of 0.55 eV. The vacancy migration energies of the EAM potentials have approximately the same magnitude, the Simonelli potential (0.46 eV) giving the lowest value and the Ackland potential (0.63 eV) giving the highest value. The migration energies obtained by the dynamical method are significantly lower than the values given by the authors of the EAM potentials in the respective publications (0.78, 0.62 and 0.84 eV, for the Ackland, Mendelev and Dudarev potential). The reason for this is that, in the original publications, $\Delta E_{\mathrm{v}}^{\mathrm{m}}$ has been determined by employing purely static calculations, where an atom is displaced from its original position to the position of the vacancy and the maximum energy along this path is taken as the migration barrier. It is noteworthy that the dynamical approach for calculating $\Delta E_{\mathrm{v}}^{\mathrm{m}}$ is usually more reliable and, in the present case, consistently leads to a better agreement with experiment for all potentials.

For the migration energy of SI atoms in bcc iron, the Simonelli and Ackland potentials give very low values of only 0.03 eV and 0.04 eV, respectively. In contrast, the Mendelev and Dudarev potentials as well as the ABOP predict higher migration energies of 0.18, 0.15 and 0.17 eV, respectively. These values are closer, but still below the experimentally determined SI migration energies of 0.25 to 0.3 e [4]. Again, the migration energies calculated by the dynamic method are lower than those from static calculations. In [57], Willaime and co-workers calculated the migration energies for the Ackland and Mendelev potentials and obtained values of 0.18 eV and 0.31 eV, respectively.

Direction-specific threshold displacement energies needed for displacing an atom in bcc iron in order to create a stable Frenkel pair have been calculated for the Simonelli, Ackland and Mendelev potentials by Nordlund *et al* [44]. Using the same method as in [44], the threshold displacement energies predicted by the ABOP have also been analysed by Nordlund [47]. The results are summarized in table 3 together with reference data from experiment [43, 42]. Although the ⟨110⟩ threshold energy is somewhat underestimated, a good agreement of the ABOP with experiments is achieved. While the minimum threshold is in the ⟨100⟩ direction, a clearly higher threshold in the ⟨110⟩ than in the ⟨111⟩ direction is obtained. A similar accordance is only provided by the Simonelli potential. Note however that the latter predicts the wrong ⟨111⟩ dumbbell as the most stable interstitial configuration.

FCC γ-iron. Owing to the thermal instability of the fcc phase in the Mendelev and Dudarev potentials, no point defect migration parameters can be calculated for these potentials. The Simonelli and Ackland potentials as well as the ABOP show very similar behaviour concerning the vacancy migration in fcc Fe. The diffusivity data are best fitted by migration energies of 0.27, 0.30 and 0.32 eV, respectively. For the SI diffusion in fcc Fe, migration energies of 0.13, 0.21 and 0.40 eV are obtained.

In summary, the ABOP provides an overall excellent description of point defects in bcc iron. The agreement with respect to static and dynamic interstitial properties is even more remarkable when considering that none of the SI properties have been used for the fitting procedure of the potential. For fcc iron, too little experimental data exists for a quantitative comparison of the potentials with the real γ-iron system. All potentials featuring a thermally stable fcc phase give, however, a description of point defect properties that is consistent amongst each other.

4. Summary

We have applied an established bond-order formalism in order to devise a new angular-dependent interatomic potential for iron. The classical treatment of the iron system that exhibits phase transitions from the α to the γ and δ phases before melting has been a challenging

problem for a long time. The new ABOP simultaneously provides an excellent description of iron both in the bcc and fcc phases. This already marks an improvement over many analytic potentials fitted solely to the bcc structure, as these often exhibit an instability of fcc iron at elevated temperatures. Moreover, in order to mimic the magnetic contributions to phase stability, we consider the static lattice energy difference between bcc and fcc iron as an adjustable quantity that is used for fitting the difference in Gibbs free energies between the corresponding phases. To our best knowledge, the present ABOP is therefore the first potential that properly reproduces the $\alpha-\gamma-\delta$ transition sequence.

Despite these improvements, the complexity of the iron phase diagram still provides room for further enhancements. In particular, this concerns the description of the hcp phase. The higher atomic volume of the hcp structure compared to the bcc structure leads to an incorrect pressure dependence of the iron phase diagram obtained from the ABOP. Note however that, apart from the Dudarev potential, this problem holds equally true for the EAM potentials analysed in this work. Also, since all potentials predict identical atomic volumes for the fcc and hcp structures, the vibrational entropy contributions to the Gibbs free energies of the fcc and hcp phases are almost identical.

In addition to the phase diagram, the new potential also performs well in describing a large variety of properties of iron in the bcc and fcc phases. The calculated phonon dispersion curves for bcc and fcc iron are in good agreement with experimental values. The formation energies of various point defects compare very well to literature data with the $\langle 110 \rangle$-interstitial as most stable configuration in bcc iron. Diffusivities obtained from MD simulations are in line with experimental results. The same holds true for the threshold displacement energy. The Bain path exhibits an energy barrier for the fcc–bcc transition that is comparable to DFT results, while all central-force potentials considered here have a lower barrier.

This potential should be suitable for modelling phase transformations, plastic deformation, fracture and other processes in iron. Because of the modularity of the functional form it can be extended to account for alloys such as Fe–Ni or Fe–C solid solutions.

Acknowledgments

Appendix. Phase stability of bcc and fcc iron

In this work, the coupling-parameter method is employed for calculating the Helmholtz free energy of a solid at a temperature T_0 [52]. An energy function $\tilde{U}$ is constructed by coupling the potential energy function of the solid of interest U to the potential energy function of a reference system U_{ref} with known free energy F_{ref}:

$$\tilde{U}(\lambda) = (1 - \lambda)U + \lambda U_{\text{ref}}. \tag{A.1}$$

The coupling parameter λ allows a gradual switching between the energy functions contributing to $\tilde{U}$. For $\lambda = 0$, the interactions of the original solid of interest are recovered, while for $\lambda = 1$, the reference system is obtained. By calculating the work required for switching between the

reference system and the solid of interest, the Helmholtz free energy of the solid F can be calculated [52]:

$$F = F_{\text{ref}} - \int_{\lambda=0}^{\lambda=1} d\lambda \langle \Delta U \rangle_\lambda, \tag{A.2}$$

with $\Delta U = U_{\text{ref}} - U$. Here, it is assumed that the switch can be performed reversibly, meaning that the switching path is free from phase transitions.

For applying the coupling-parameter method to free energy calculations of solids, the Einstein crystal is a convenient choice for a reference system. The atoms in a classical Einstein crystal do not interact with each other; instead they are coupled harmonically to their equilibrium lattice positions $\mathbf{r}_{0,i}$ via a spring constant α. The potential energy function U_{ref} of the Einstein crystal of N atoms then reads

$$U_{\text{ref}}(\mathbf{r}^N) = \tfrac{1}{2}\alpha \sum_{i=1}^{N} (\mathbf{r}_i - \mathbf{r}_{0,i})^2. \tag{A.3}$$

Since the atoms in an Einstein crystal do not experience any interatomic interactions, no pressure can be defined and calculations can only be carried out in the N, V, T ensemble.

In practice, the integrand in (A.2) is evaluated by a series of MC simulations at different values for λ and the integral is evaluated numerically. For obtaining a smooth integrand and therefore enhancing the accuracy of the numerical integration, the spring constant α is adjusted so that the mean-square displacement in the Einstein crystal equals the mean-square displacement $\langle \Delta r^2 \rangle$ in the solid: $\alpha = 3k_BT/\langle \Delta r^2 \rangle$ [52]. Also for numerical reasons, the sampling of the integrand in (A.2) is conducted under the fixed centre of mass constraint [58, 52]. Correcting for finite-size effects and including the fixed centre of mass constraint, the Helmholtz free energy of the solid of interest can finally be written as [59]

$$\frac{F}{Nk_BT} = -\frac{3}{2}\ln\left(\frac{k_B^2 T^2 m}{\hbar^2 \alpha}\right) - \frac{1}{Nk_BT}\int_0^1 d\lambda \langle \Delta U \rangle_\lambda$$
$$- \frac{3}{2N}\ln\left(\frac{\alpha}{2\pi k_BT}\right) - \frac{3}{2N}\ln N + \frac{1}{N}\ln\frac{N}{V}. \tag{A.4}$$

Here, V is the volume of the system, m the atomic mass and $\hbar$ denotes Planck's constant[2].

In order to compare the thermodynamic stabilities of the bcc and fcc phases of the analytic potentials, the phase with the lower Gibbs free energy G has to be identified. For calculating G with the Einstein crystal as the reference system, the coupling-parameter method has been used as described in the following. As a first step, the equilibrium volume V_0 at temperature T_0 and zero pressure is determined by an MD simulation run. The spring constant α of the reference Einstein crystal is then adjusted to the $\langle \Delta r^2 \rangle$ obtained from a MC simulation at constant V_0 and coupling parameter $\lambda = 0$. The integrand in (A.2) is then evaluated by a series of fixed centre of mass MC simulations for λ varying from 0 to 1 with an interval of $\Delta\lambda = 0.05$. The system sizes used for the calculations are $8 \times 8 \times 8$ unit cells for the bcc lattice and $6 \times 6 \times 7$ unit cells for the fcc lattice, which corresponds to 1024 and 1008 atoms, respectively. For each λ, the value of $\Delta U(\mathbf{r}^N)$ is sampled over at least 5000 MC steps after allowing the system to equilibrate for 500 MC steps.

The temperature dependence of the Gibbs free energy can in principle be obtained by applying the coupling-parameter method at different temperatures T_0. Alternatively, integrating the Gibbs–Helmholtz equation offers a computationally more efficient approach. Once the

---

[2] In [59], Planck's constant is omitted in the first term on the right-hand side of (A.4).

Gibbs free energy G_0 has been determined by the coupling-parameter method at an arbitrary T_0, the Gibbs free energy at any other temperature is obtained by

$$\frac{G(T)}{T} = \frac{G(T_0)}{T_0} - \int_{T_0}^{T} \frac{H(\tau)}{\tau^2} \, d\tau, \tag{A.5}$$

where $H(\tau)$ denotes the enthalpy at temperature τ. In this work, Gibbs free energies of the bcc and fcc iron phases have therefore been determined by applying the coupling-parameter method once for $T_0 = 300$ K or alternatively 600 K and by integrating the Gibbs–Helmholtz equation for other temperatures using $H(T)$ data gained from MD simulations in 25 K intervals up to the melting point.

The accuracy of the integration and moreover the correctness of the implementation of the coupling-parameter method can be verified by repeating the coupling-parameter method at a few selected temperatures, which provides Gibbs free energy data from two (apart from the value at T_0) independent sources. Our calculations show that the maximum deviation between the two methods for the absolute value of the free energy is less than 5 meV/atom. Furthermore, for free energy differences between two solid phases, the deviation is less than 0.4 meV/atom.

References

[1] Daw M S and Baskes M I 1984 *Phys. Rev.* B **29** 6443
[2] Cleri F and Rosato V 1993 *Phys. Rev.* B **48** 22
[3] Baskes M I 1992 *Phys. Rev.* B **46** 2727
[4] Ehrhart P 1991 *Landolt–Börnstein: Numerical data and Functional Relationships in Science and Technology* vol III (Heidelberg: Springer)
[5] Hasegawa H and Pettifor D G 1983 *Phys. Rev. Lett.* **50** 130
[6] Simonelli G, Pasianot R and Savino E J 1993 *Mater. Res. Soc. Symp. Proc.* **291** 567
[7] Ackland G J, Bacon D J, Calder A F and Harry T 1997 *Phil. Mag.* A **75** 713
[8] Meyer R and Entel P 1998 *Phys. Rev.* B **57** 5140
[9] Osetsky Y N and Serra A 1998 *Phys. Rev.* B **57** 755
[10] Mendelev M I, Han S, Srolovitz D J, Ackland G J, Sun D Y and Asta M 2003 *Phil. Mag.* **83** 3977
[11] Dudarev S L and Derlet P M 2005 *J. Phys.: Condens. Matter* **17** 7097
[12] Chamati H, Papanicolaou N, Mishin Y and Papaconstantopoulos D 2006 *Surf. Sci.* **600** 1793–803
[13] Lee B J, Baskes M I, Kim H and Cho Y K 2001 *Phys. Rev.* B **64** 184102
[14] Simonelli G, Pasianot R and Savino E J 1997 *Phys. Rev.* B **55** 5570
[15] Mishin Y, Mehl M and Papaconstantopoulos D 2005 *Acta Mater.* **53** 4029
[16] Albe K, Nordlund K and Averback R S 2002 *Phys. Rev.* B **65** 195124
[17] Juslin N, Erhart P, Traskelin P, Nord J, Henriksson K, Nordlund K, Salonen E and Albe K 2005 *J. Appl. Phys.* **98** 3520
[18] Albe K, Nordlund K, Nord J and Kuronen A 2002 *Phys. Rev.* B **66** 035205
[19] Robertson I J, Heine V and Payne M C 1993 *Phys. Rev. Lett.* **70** 1944
[20] Mishin Y, Farkas D, Mehl M J and Papaconstantopoulos D A 1999 *Phys. Rev.* B **59** 3393
[21] Erhart P and Albe K Pontifix/Pinguin: A program package for fitting interatomic potentials of the bond-order type *Comp. Mater. Sci.* submitted http://www.mm.mw.tu-darmstadt.de/
[22] Kresse G and Furthmüller J 1996 *Phys. Rev.* B **54** 11169
[23] Blöchl P E 1994 *Phys. Rev.* B **50** 17953–79
[24] Kresse G and Joubert D 1999 *Phys. Rev.* B **59** 1758–75
[25] Perdew J P 1991 *Electronic Structure of Solids* ed P Ziesche and H Eschrig (Berlin: Akademie)
[26] Birch F 1978 *J. Geograph. Res.* **83** 1257
[27] Herper H C, Hoffmann E and Entel P 1999 *Phys. Rev.* B **60** 3839
[28] Herper H C, Hoffmann E and Entel P 2002 *Phase Transit.* **75** 185
[29] Acet M, Zähres H, Wassermann E F and Pepperhoff W 1994 *Phys. Rev.* B **49** 6012
[30] Purdum H, Montano P A, Shenoy G K and Morrison T 1982 *Phys. Rev.* B **25** 4412
[31] Miedema A R and Gingerich K A 1979 *J. Phys. B: At. Mol. Phys.* **12** 2081
[32] Lian L, Su C X and Armentrout P B 1992 *J. Chem. Phys.* **97** 4072
[33] Moskovits M and DiLella D P 1980 *J. Chem. Phys.* **73** 4917

[34] Gutsev G L, Mochena M D, Jena P, Bauschlicher C W Jr and Partridge H III 2004 *J. Chem. Phys.* **121** 6785
[35] Kittel C 1986 *Introduction to Solid State Physics* 6th edn (New York: Wiley)
[36] Lide D R (ed) 2004 *Handbook of Chemistry and Physics* 85th edn (Boca Raton, FL: CRC Press)
[37] Chen S and Sundman B 2001 *J. Phase Equilib.* **22** 631
[38] Clatterbuck D M, Chrzan D C and Morris J W Jr 2003 *Acta Mater.* **51** 2271
[39] Zarestky J and Stassis C 1987 *Phys. Rev.* B **35** 4500
[40] Domain C and Becquart C S 2002 *Phys. Rev.* B **65** 024103
[41] Fu C C, Willaime F and Ordejón P 2004 *Phys. Rev. Lett.* **92** 175503
[42] Maury F, Biget M, Vajda P, Lucasson A and Lucasson P 1976 *Phys. Rev.* B **14** 5303
[43] Lomer J N and Pepper M 1967 *Phil. Mag.* **16** 1119
[44] Nordlund K, Wallenius J and Malerba L 2006 *Nucl. Instrum. Methods Phys. Res.* B **246** 322
[45] Becquart C S, Domain C, Legris A and van Duysen J C 2000 *J. Nucl. Mater.* **280** 73
[46] Becquart C S, Domain C, Legris A and van Duysen J C 2001 *Mater. Res. Soc. Symp. Proc.* **650** R3.24.1
[47] Nordlund K, private communication
[48] Tyson W R and Miller W A 1977 *Surf. Sci.* **62** 267
[49] Spencer M J S, Hung A, Snook I K and Yarovsky I 2002 *Surf. Sci.* **513** 389
[50] Yan J A, Wang C Y and Wang S Y 2004 *Phys. Rev.* B **70** 174105
[51] Kim S M and Buyers W J L 1978 *J. Phys. F: Met. Phys.* **8** L103
[52] Frenkel D and Smit B 1996 *Understanding Molecular Simulation: From Algorithms to Applications* (New York: Academic)
[53] Lopasso E M, Caro M, Caro A and Turchi P 2003 *Phys. Rev.* B **68** 214205
[54] Caro A, Caro M, Lopasso E M, Turchi P E A and Farkas D 2006 *J. Nucl. Mater.* **349** 317
[55] Klotz S and Braden M 2000 *Phys. Rev. Lett.* **85** 3209
[56] Nguyen-Manh D, Horsfield A P and Dudarev S L 2006 *Phys. Rev.* B **73** 020101(R)
[57] Willaime F, Fu C, Marinica M and Dalla Torre J 2005 *Nucl. Instrum. Methods Phys. Res.* B **228** 92–9
[58] Frenkel D and Ladd A J C 1984 *J. Chem. Phys.* **81** 3188
[59] Polson J M, Trizac E, Pronk S and Frenkel D 2000 *J. Chem. Phys.* **112** 5339